A&A 599, A135 (2017)
DOI: 10.1051/0004-6361/201629954


Astronomy & Astrophysics

# *Odin* observations of ammonia in the Sgr A +50 km s$^{-1}$ cloud and circumnuclear disk[⋆,⋆⋆]

Aa. Sandqvist[1], Å. Hjalmarson[2], U. Frisk[3], S. Lundin[4], L. Nordh[1], M. Olberg[5], and G. Olofsson[1]

[1] Stockholm Observatory, Stockholm University, AlbaNova University Center, 106 91 Stockholm, Sweden
e-mail: aage@astro.su.se
[2] Department of Earth and Space Sciences, Chalmers University of Technology, Onsala Space Observatory, 439 92 Onsala, Sweden
[3] Omnisys Instruments AB, Solna Strandväg 78, 171 54 Solna, Sweden
[4] OHB Sweden, PO Box 1269, 164 29 Kista, Sweden
[5] Onsala Space Observatory, Chalmers University of Technology, 439 92 Onsala, Sweden

Received 25 October 2016 / Accepted 21 December 2016

**ABSTRACT**

*Context.* The *Odin* satellite is now into its sixteenth year of operation, much surpassing its design life of two years. One of the sources which *Odin* has observed in great detail is the Sgr A complex in the centre of the Milky Way.
*Aims.* To study the presence of $NH_3$ in the Galactic centre and spiral arms.
*Methods.* Recently, *Odin* has made complementary observations of the 572 GHz $NH_3$ line towards the Sgr A +50 km s$^{-1}$ cloud and circumnuclear disk (CND).
*Results.* Significant $NH_3$ emission has been observed in both the +50 km s$^{-1}$ cloud and the CND. Clear $NH_3$ absorption has also been detected in many of the spiral arm features along the line of sight from the Sun to the core of our Galaxy.
*Conclusions.* The very large velocity width (80 km s$^{-1}$) of the $NH_3$ emission associated with the shock region in the southwestern part of the CND may suggest a formation/desorption scenario similar to that of gas-phase $H_2O$ in shocks/outflows.

**Key words.** Galaxy: center – ISM: individual objects: Sgr A – ISM: molecules – ISM: clouds

## 1. Introduction

The core of the Milky Way Galaxy is a region of great complexity containing a wide variety of physical environments. At the very centre resides a four-million-solar-mass supermassive black hole, whose non-thermal radio continuum signature is called Sgr A$^*$. Orbiting around it, at a distance of one to a few pc, with a velocity of about 100 km s$^{-1}$, is a molecular torus called the circumnuclear disk (CND). The CND has a mass of $10^4$ to $10^5$ $M_\odot$ and a gas temperature of several hundred degrees. Beyond this, there exists a large Molecular Belt consisting predominantly of two GMCs, called the +50 and the +20 km s$^{-1}$ clouds. Both GMCs are massive, about $5 \times 10^5$ $M_\odot$, with a density $10^4$–$10^5$ cm$^{-3}$, gas temperature 80–100 K, and dust temperature 20–30 K (e.g. Sandqvist et al. 2008). General reviews of the centre have been presented by e.g. Mezger et al. (1996) and Morris & Serabyn (1996), with an up-to-date introduction to the Sgr A complex given by Ferrière (2012).

The *Odin* satellite (Nordh et al. 2003; Frisk et al. 2003) has surveyed the Sgr A complex in a number of different molecules. While it was unsuccessful in searching for $O_2$ – a 3$\sigma$ upper limit for the fractional abundance ratio of [$O_2$/$H_2$], averaged over a 9-arcmin region, was found to be $X(O_2) \leq 1.2 \times 10^{-7}$ (Sandqvist et al. 2008) – significant amounts of $H_2O$, CO and C I were detected in many regions of the Sgr A complex (Karlsson et al. 2013). Unfortunately, there were a number of instabilities in the 572 GHz $NH_3$ receiver during those observation periods which prevented us from obtaining results for this $NH_3$ transition in the core region of the Galaxy, although some results were obtained for the spiral arm features. These instabilities were due to a loss of phase lock for this receiver early in the mission. However, with appropriate centering of the observing frequency and many frequency calibrations, performed using a nearby telluric ozone line, it is possible to correct for this lack of phase lock. This short paper now reports on new successful *Odin* $NH_3$ observations in the Sgr A +50 km s$^{-1}$ cloud, and in the southwestern region of the CND which is a complex shocked region containing a number of interacting components (Karlsson et al. 2015).

## 2. Observations

The *Odin* observations of the o-$NH_3$ ($1_0$–$0_0$) line at 572.4981 GHz towards the Sgr A +50 km s$^{-1}$ cloud at J2000.0 $17^h45^m51\overset{s}{.}7$, $-28°59'09''$ were performed in April 2015, with an ON-source total integration time of 27.4 h. The $NH_3$ observations towards the southwestern (SW) lobe of the Sgr A CND at J2000.0 $17^h45^m39\overset{s}{.}7$, $-29°01'18''$ were performed in April 2016, with an ON-source total integration time of 26.7 h. The system temperatures were 3300 and 3400 K, respectively. The halfpower beamwidth of *Odin* at the $NH_3$ frequency is $2\overset{'}{.}1$ and the main beam efficiency is 0.89 (Frisk et al. 2003). The backend spectrometer was a 1050 MHz AOS with a channel resolution of 1 MHz. For more details of *Odin* Galactic centre observations, see Karlsson et al. (2013).

⋆ *Odin* is a Swedish-led satellite project funded jointly by the Swedish National Space Board (SNSB), the Canadian Space Agency (CSA), the National Technology Agency of Finland (Tekes), the Centre National d'Études Spatiales (CNES), France, and the European Space Agency (ESA). The former Space division of the Swedish Space Corporation, today OHB Sweden, is the prime contractor, also responsible for *Odin* operations.
⋆⋆ The reduced spectra are only available at the CDS via anonymous ftp to cdsarc.u-strasbg.fr (130.79.128.5) or via http://cdsarc.u-strasbg.fr/viz-bin/qcat?J/A+A/599/A135

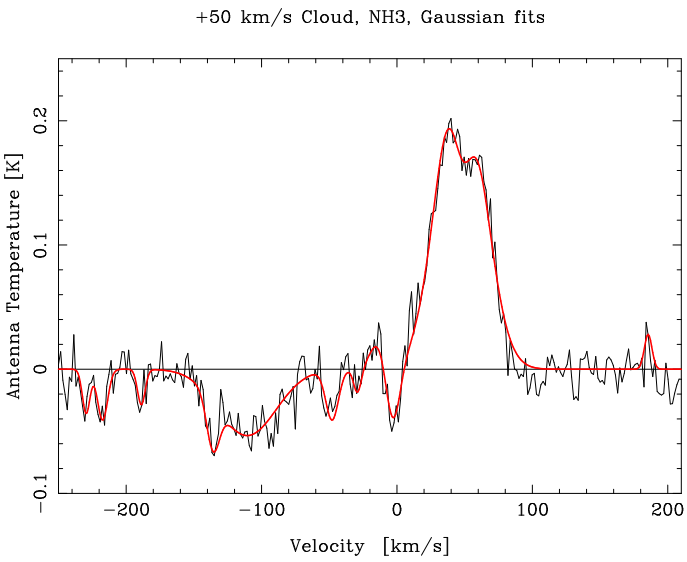


**Fig. 1.** *Odin* observations of the 572 GHz $NH_3$ line towards the Sgr A +50 km s$^{-1}$ cloud (black profile); the channel resolution is 1.6 km s$^{-1}$. The red profile is the result of the Gaussian analysis.

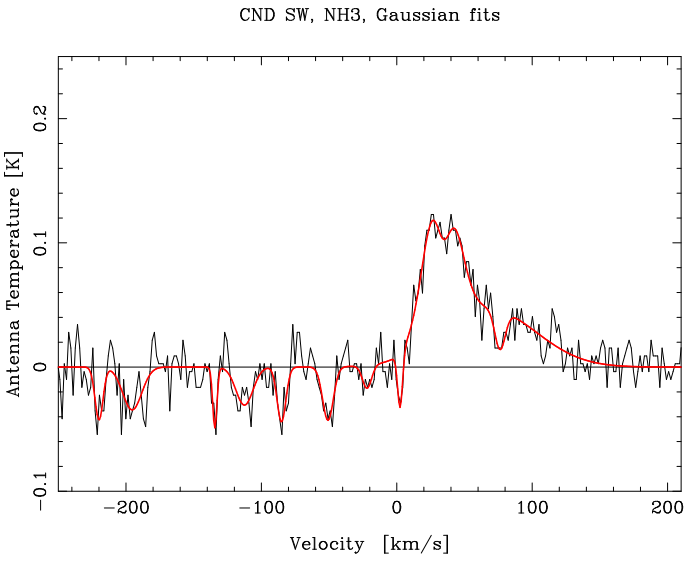


**Fig. 2.** *Odin* observations of the 572 GHz $NH_3$ line towards the south-western part of the Sgr A circumnuclear disk (black profile); the channel resolution is 1.6 km s$^{-1}$. The red profile is the result of the Gaussian analysis.

## 3. Results and discussion

Our two $NH_3$ profiles, obtained towards the +50 km s$^{-1}$ cloud and the CND SW, are presented in Figs. 1 and 2, where they have been smoothed to a channel resolution of 1.6 km s$^{-1}$. Gaussian analysis was performed on both profiles by visual estimation of all three parameters (intensity, velocity, and velocity half width) for each emission and absorption component and the fit was then executed in an unbiased manner. The Gaussian analysis fittings are also presented in Figs. 1 and 2, and in Tables 1 and 2 where the listed uncertainties are at the 1$\sigma$ level. The dominant impression in the figures is the clear emission features at positive velocities, which arise in the Sgr A complex (e.g. Sandqvist 1989). Most of the numerous weaker absorption features at negative velocities are caused by the various Galactic spiral arm components along the line of sight from the Sun to the Galactic centre and are identifiable by their radial velocities (Sandqvist et al. 2015). A few of these features are near the limit of detectability, but correspond to clearly identifiable signatures observed in e.g. OH, $H_2O$ and CO lines presented by Karlsson et al. (2013). The rms noise levels in the two profiles are 9 and 11 mK, respectively, so the intensities of the weak absorption features are predominantly greater than 3$\sigma$.

The very fact that we are only observing ground-state ammonia absorption features at negative velocities, and see no visible emission, against very weak continuum background sources (only 210 and 140 mK) implies that the excitation temperature ($T_{ex}$) of this gas must be close to the temperature of the cosmic microwave background ($T_{CMB}$ = 2.725 K), which means that the dominant part of the ammonia population is residing in the lowest state. This also means that the absorbing gas regions must have a density several orders of magnitude lower than the critical density of the ammonia line ($5 \times 10^7$ cm$^{-3}$), which is also consistent with their low $H_2$ column densities (see Table 3) and low visual extinction. From the Gaussian analysis of the absorption features, we can now obtain column densities, $N(NH_3)$, of ortho-$NH_3$ in a manner similar to Karlsson et al. (2013):

$$N(NH_3) = 3.69 \times 10^{12} \tau_o(NH_3) \Delta V_{FWHM} \quad (1)$$

where $\Delta V_{FWHM}$ is the line full width at half maximum and $\tau_o$ is the central optical depth of the Gaussian fitted to the absorption feature and (for $T_{ex} = T_{CMB}$) can be calculated as

$$\tau_o = -\ln\left[1 + \frac{T_A^*}{T_{cont}}\right]. \quad (2)$$

In Eq. (2), $T_A^*$ is the antenna temperature of the absorption line intensity and is a negative number and $T_{cont}$ is the background continuum temperature, which is 210 and 140 mK for the +50 km s$^{-1}$ cloud and the CND SW, respectively (Karlsson et al. 2013). The results of the Gaussian analysis of the absorption features are summarized in Tables 1 and 2.

The major emission feature in the +50 km s$^{-1}$ profile, at 47 km s$^{-1}$ originates *in* the +50 km s$^{-1}$ cloud. The Gaussian analysis yielded a $T_A^*$ = 266 mK and a line width of 39 km s$^{-1}$. Correcting for the beam efficiency (0.89) we obtain a main beam brightness temperature of 298 mK. In order to obtain an $NH_3$ column density for the cloud, we have used the on-line version of RADEX[1] (van der Tak et al. 2007). Assuming a gas temperature of $T$ = 80 K and a gas density of $n_{H_2} = 10^4$ cm$^{-3}$ (Walmsley et al. 1986; Sandqvist et al. 2008) and a line width of 39 km s$^{-1}$, we get $N(NH_3) = 1 \times 10^{16}$ cm$^{-2}$. This is comparable to the value of $2 \times 10^{16}$ deduced by Mills & Morris (2013) from their observations of 14 higher $NH_3$ transitions in this cloud, where they estimate that about 10% of the $NH_3$ column originates from a high temperature (≈400 K) cloud component. It is, however, larger than the value of $3 \times 10^{15}$ cm$^{-2}$ obtained by Herrnstein & Ho (2005) from their observations of the 23 GHz inversion line. For the +50 km s$^{-1}$ cloud, our column density value then yields an o-$NH_3$ abundance with respect to hydrogen, $X(NH_3) = N(NH_3)/N(H_2)$, of $4 \times 10^{-8}$, if we assume a molecular hydrogen column density of $N(H_2) = 2.4 \times 10^{23}$ cm$^{-2}$ (Lis & Carlstrom 1994), which was determined from observations of a total dust column. Using instead the value of $N(H_2) = 1.6 \times 10^{23}$ cm$^{-2}$, which was determined from SEST observations of the $C^{18}O$ (1–0) and (2–1) lines at this position, (Karlsson et al. 2013), we get an o-$NH_3$ abundance of $6.3 \times 10^{-8}$.

[1] http://var.sron.nl/radex/radex.php

**Table 1.** Gaussian fits to the +50 km s$^{-1}$ cloud $NH_3$ profile.

| $V$ (km s$^{-1}$) | $T_A^*$ (mK) | $\Delta V$ (km s$^{-1}$) | $\tau_o$ | $N(NH_3)$ (cm$^{-2}$) | Source |
|---|---|---|---|---|---|
| −230 | −36 ± 8 | 7 | 0.19 ± 0.05 | $(5 \pm 1) \times 10^{12}$ | High Negative Velocity Gas (HNVG) |
| −217 | −41 ± 7 | 9 | 0.22 ± 0.04 | $(7 \pm 1) \times 10^{12}$ | HNVG |
| −189 | −29 ± 8 | 7 | 0.15 ± 0.04 | $(4 \pm 1) \times 10^{12}$ | HNVG |
| −136 | −39 ± 8 | 11 | 0.21 ± 0.04 | $(8 \pm 2) \times 10^{12}$ | Expanding Molecular Ring (EMR) (near side) |
| −111 | −53 ± 3 | 51 | 0.29 ± 0.02 | $(55 \pm 3) \times 10^{12}$ | EMR (near side) |
| −48 | −40 ± 6 | 11 | 0.21 ± 0.03 | $(9 \pm 1) \times 10^{12}$ | 3-kpc arm |
| −29 | −19 ± 9 | 7 | 0.10 ± 0.04 | $(2 \pm 1) \times 10^{12}$ | −30 km s$^{-1}$ arm |
| −3 | −45 ± 39 | 12 | 0.24 ± 0.20 | $(10 \pm 9) \times 10^{12}$ | Local/Sgr arm |
| 47 | 266 ± 29 | 39 | ... | $(1 \pm 0.1) \times 10^{16}$ | +50 km s$^{-1}$ cloud[a] |
| 49 | −96 ± 28 | 18 | 0.23 ± 0.07 | $(15 \pm 5) \times 10^{12}$ | +50 km s$^{-1}$ cloud[b] |
| 186 | 28 ± 8 | 7 | ... | ... | ... |

**Notes.** [(a)] From RADEX analysis, see text; [(b)] Self-absorption, see text.

**Table 2.** Gaussian fits to the CND SW $NH_3$ profile.

| $V$ (km s$^{-1}$) | $T_A^*$ (mK) | $\Delta V$ (km s$^{-1}$) | $\tau_o$ | $N(NH_3)$ (cm$^{-2}$) | Source |
|---|---|---|---|---|---|
| −220 | −43 ± 8 | 7 | 0.36 ± 0.08 | $(9 \pm 2) \times 10^{12}$ | HNVG |
| −195 | −34 ± 5 | 17 | 0.28 ± 0.05 | $(17 \pm 3) \times 10^{12}$ | HNVG |
| −134 | −49 ± 12 | 4 | 0.43 ± 0.13 | $(6 \pm 2) \times 10^{12}$ | EMR (near side) |
| −113 | −31 ± 6 | 15 | 0.25 ± 0.05 | $(14 \pm 3) \times 10^{12}$ | EMR (near side) |
| −85 | −44 ± 8 | 8 | 0.38 ± 0.08 | $(11 \pm 2) \times 10^{12}$ | CND |
| −51 | −43 ± 7 | 9 | 0.37 ± 0.07 | $(13 \pm 2) \times 10^{12}$ | 3-kpc arm |
| −22 | −19 ± 8 | 8 | 0.14 ± 0.06 | $(4 \pm 2) \times 10^{12}$ | −30 km s$^{-1}$ arm |
| 3 | −44 ± 11 | 4 | 0.38 ± 0.11 | $(6 \pm 2) \times 10^{12}$ | Local/Sgr arm |
| 33 | 139 ± 47 | 27 | ... | $(4 \pm 1) \times 10^{15}$ | Molecular Belt[a] |
| 34 | −64 ± 50 | 13 | 0.23 ± 0.19 | $(11 \pm 9) \times 10^{12}$ | Molecular Belt[b] |
| 68 | 46 ± 6 | 81 | ... | $(7 \pm 1) \times 10^{14}$ | Shock region[a] |
| 76 | −31 ± 8 | 9 | 0.19 ± 0.05 to 1.18 ± 0.6 | $((6 \pm 2)$ to $(40 \pm 20)) \times 10^{12}$ | ??[b] |

**Notes.** [(a)] From RADEX analysis, see text; [(b)] Self-absorption, see text.

The emission profile of the +50 km s$^{-1}$ cloud is significantly affected by self-absorption, as can be seen in Fig. 1. Also, the Gaussian analysis resulted in a clear self-absorption feature at 49 km s$^{-1}$ (see Table 1) with an intensity of −96 mK. The corresponding optical depth and column density for this feature were then determined, using Eqs. (2) and (1), assuming that the self-absorbing region of the cloud is on the near side of the +50 km s$^{-1}$ cloud and thus absorbing both the background continuum of 210 mK and the background line emission of 265 mK, a total of 475 mK.

There are two overlapping emission features in the CND SW profile seen in Fig. 2 and analysed in Table 2, namely at 33 and 68 km s$^{-1}$ with line widths of 27 and 81 km s$^{-1}$, respectively. In both of these features there are signs of self-absorption at 34 and 76 km s$^{-1}$, respectively. The optical depths of these self-absorptions will depend on the relative positions of the components along the line of sight. For the 34 km s$^{-1}$ self-absorption we determine the optical depth, assuming that it and its emission companion at 33 km s$^{-1}$ are in front of the emission component at 76 km s$^{-1}$, and that the self-absorption is on the near side of the 33 km s$^{-1}$ component. Thus the self-absorbing region absorbs the continuum emission of 140 K and both the 33 km s$^{-1}$ emission and the blue overlapping wing of the 68 km s$^{-1}$ emission feature, which amounts to a total sum of 140 + 138 + 28 = 306 mK, a value we use for $T_{cont}$ in Eq. (2). For the 76 km s$^{-1}$ self-absorption, we assume that the self-absorbing region is on the near side of the 68 km s$^{-1}$ emission region and both lie either in front of, or behind, the 140 K continuum region. Thus a range for the optical depth is obtained, using either the red-shifted emission of the 68 km s$^{-1}$ region at the appropriate velocity of 76 km s$^{-1}$ whose emission value is 45 mK, or 140 + 45 = 185 mK, the values of which we use for $T_{cont}$ in Eq. (2).

There are two major emission features in the CND SW profile and we have performed a RADEX analysis of both. First we assume that the 33 km s$^{-1}$ feature originates in the Molecular Belt and we can thus apply its physical properties to the analysis, namely a gas temperature of 80 K and density of $10^4$ cm$^{-3}$. The antenna temperature of 139 mK converts to a main beam temperature of 156 mK; the line width is 27 km s$^{-1}$. The best RADEX fit then yields an $NH_3$ column density of $4 \times 10^{15}$ cm$^{-2}$.

Perhaps the most interesting feature is the broad $NH_3$ emission feature centered at 68 km s$^{-1}$ with a line width of 81 km s$^{-1}$. *Odin* has detected a comparable very broad $H_2^{18}O$ absorption line at the same position (Karlsson et al. 2015) – see Fig. 3. The antenna temperature of this $NH_3$ feature is 46 mK, which implies a main beam temperature of 52 mK. Applying a RADEX study, and assuming a kinetic temperature of 200 K and density

**Table 3.** $NH_3$ and $H_2O$ abundance comparisons.

| Source | $N(NH_3)$ ($cm^{-2}$) | $N(H_2)$ ($cm^{-2}$) | $X(NH_3)$ ($\times 10^{-9}$) | $X(H_2O)$ ($\times 10^{-9}$) |
|---|---|---|---|---|
| *Sgr A complex components* | | | | |
| +50 km s$^{-1}$ cloud | $(1 \pm 0.1) \times 10^{16}$ | $1.6 \times 10^{23}$[a] | 63 | 40[a] |
| +50 km s$^{-1}$ cloud red wing | ... | ... | ... | ≥1000[a] |
| Molecular Belt at CND SW | $(4 \pm 1) \times 10^{15}$ | $<1.0 \times 10^{23}$[b] | >40 | ... |
| Shock region at CND SW | $(7 \pm 1) \times 10^{14}$ | $4 \times 10^{22}$[c] | 18 | 1400[c] |
| +20 km s$^{-1}$ cloud | ... | $1 \times 10^{23}$[b] | ... | 20[a] |
| +20 km s$^{-1}$ cloud red wing | ... | ... | ... | ≥800[a] |
| *Galactic components* | | | | |
| EMR | $(30 \pm 2) \times 10^{12}$[d] | $2.5 \times 10^{21}$[e] | 12 | ... |
| 3-kpc Arm | $(11 \pm 2) \times 10^{12}$[d] | $4.0 \times 10^{21}$[f] | 3 | >3[f] |
| −30 km s$^{-1}$ Arm | $(3 \pm 1) \times 10^{12}$[d] | $1.9 \times 10^{21}$[f] | 2 | 30[a] |
| Local/Sgr Arm | $(8 \pm 5) \times 10^{12}$[d] | $6.4 \times 10^{21}$[f] | 1 | >3[f] |

**Notes.** [(a)] Karlsson et al. (2013); [(b)] value for the +20 km s$^{-1}$ cloud from Karlsson et al. (2013); [(c)] Karlsson et al. (2015); [(d)] mean of the respective values in Tables 1 and 2; [(e)] deduced from the $^{13}$CO(1−0) profile in Fig. 1a by Bally et al. (1988) and the conversion factor given by Sofue (1995); [(f)] Sandqvist et al. (2003).

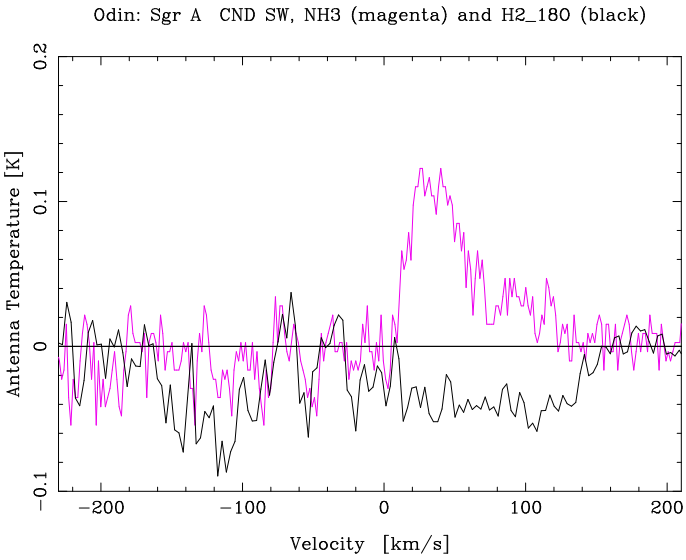


**Fig. 3.** Comparison of the *Odin* observations of the 572 GHz $NH_3$ line (magenta) and the 548 GHz $H_2^{18}O$ line (black) towards the southwestern part of the Sgr A circumnuclear disk; the channel resolutions are 1.6 and 3 km s$^{-1}$, respectively.

of $4 \times 10^4$ cm$^{-3}$ (Requena-Torres et al. 2012), we obtain a column density of o-$NH_3$ of $7 \times 10^{14}$ cm$^{-2}$. The $H_2$ column density for this region is $4 \times 10^{22}$ cm$^{-2}$ (Karlsson et al. 2015), which would then yield an abundance ratio for o-$NH_3$ with respect to $H_2$ of $X[NH_3] = 1.75 \times 10^{-8}$. Karlsson et al. (2015) obtained a strikingly high $H_2O$ abundance of $1.4 \times 10^{-6}$ in this shock region.

A summary of the derived $NH_3$ abundances for different components in the Sgr A complex and Galactic features is presented in Table 3, together with $H_2O$ abundances, where available. It appears that the ortho-ammonia abundances of $(2-6) \times 10^{-8}$ observed by us in the Sgr A molecular cloud regions (the +50 km s$^{-1}$ cloud, as well as the Molecular Belt) can be accommodated in current chemical models for dense gas clouds (Pineau des Forets et al. 1990), especially so if grain surface reactions and various subsequent desorption processes are considered (Persson et al. 2014; dense cloud part of their Fig. C2). Our detections of $NH_3$ at the much lower abundance of $(1-3) \times 10^{-9}$ in spiral arm clouds are not so easy to understand in terms of chemical models. Similarly low abundances have been derived by Persson et al. (2010, 2012) from *Herschel* observations of spiral arm $NH_3$ absorption regions in the directions of W49N and G10.6−0.4 (W31C), and by Wirström et al. (2010) from *Odin* observations in the direction of Sgr B2. The $NH_3$ abundances in diffuse or translucent clouds, estimated by Liszt et al. (2006) from 23 GHz inversion line absorption against compact extragalactic sources, are also similarly low. The low $H_2$ column densities of the spiral arm clouds correspond to only a few magnitudes of visual extinction[2] and rather low cloud densities (so called translucent clouds). However, it seems that a chemical model combining gas-phase and grain surface reactions can do the job at a temperature of 30−50 K and a density of $\approx 10^3$ cm$^{-3}$, but only if the relevant species really are desorbed as a result of exothermic surface reactions (Persson et al. 2014; their Fig. C3, and the translucent gas part of Fig. C2). A remaining concern may be that the simultaneous model abundances of NH and $NH_2$ are not consistent with those observed by Persson et al. (2010, 2012).

As discussed in some detail by Karlsson et al. (2013), the gas-phase water abundances determined for the Sgr A +50 km s$^{-1}$ and +20 km s$^{-1}$ molecular clouds are considerably enhanced compared to the situation in cold cloud cores where the water mainly resides as ice on the cold grain surfaces. Similarly high or even more enhanced water abundances have been estimated in lower density spiral arm clouds observed in absorption against Sgr A by Karlsson et al. (2013), and against Sgr B2 using *Odin* by Wirström et al. (2010) and using *Herschel* Space Observatory also by Lis et al. (2010). The elevated gas phase water abundances definitely require desorption of water ice, most likely handled by PDR modeling including grain surface reactions (cf. Hollenbach et al. 2009) The release of water molecules formed on colder grain surfaces may also explain the ortho-to-para $H_2O$ abundance ratio lower than 3 very likely observed in the spiral arms against Sgr B2 (Lis et al. 2010).

The very high gas-phase water abundance determined for the shock region at CND SW by Karlsson et al. (2015) is similar

[2] Using $N(H_2)/A_v \approx 0.94 \times 10^{21}$ cm$^{-2}$ mag$^{-1}$, Bohlin et al. (1978).

to that found in the red-ward high-velocity wings of the Sgr A molecular clouds, and likely results from shock heating causing release of pre-existing grain surface water, possibly combined with high temperature shock chemistry. (cf. discussion in Karlsson et al. 2013). The very large velocity width (80 km s$^{-1}$) of the $NH_3$ emission associated with the shock region at the CND SW (Fig. 2 and Table 2) may suggest a formation/desorption scenario similar to that of gas-phase $H_2O$ in shocks/outflows, where the actual ammonia abundance is achievable in chemical models for quiescent molecular cloud (as discussed previously).

## 4. Conclusions

We have successfully observed $NH_3$ emission from the Sgr A +50 km s$^{-1}$ cloud and the CND using the *Odin* satellite. The very large velocity width (80 km s$^{-1}$) of the $NH_3$ emission associated with the shock region in the southwestern part of the CND may suggest a formation/desorption scenario similar to that of gas-phase $H_2O$ in shocks/outflows. In addition, clear $NH_3$ absorption has also been observed in the spiral arm features along the line of sight to the Galactic centre.

The high quality *Odin* $NH_3$ spectra, observed in 2015 and 2016, presented in this short paper, together with the $H_2O$ and $H_2^{18}O$ spectra of similarly high quality observed by *Odin* towards Comet C/2014 Q2 (Lovejoy) in January – February 2015 (Biver et al. 2016) were obtained 14−15 yr after the launch of the *Odin* satellite. This demonstrates to our delight (and also some surprise) that it is possible to build a comparatively cheap, but still rather complicated, satellite observatory (with five tunable heterodyne receivers and a mechanical cooling machine) which can remain in high quality operation for 15 yr or more. We should here note that the *Odin* satellite observatory since many years has been operated practically full-time in global monitoring of the terrestrial atmosphere (the *Odin* aeronomy mode).

## References


Bally, J., Stark, A. A., Wilson, R. W., & Henkel, C. 1988, ApJ, 324, 223
Biver, N., Moreno, R., Bockelée-Morvan, D., et al. 2016, A&A, 589, A78
Bohlin, R. C., Savage, B. D., & Drake, J. F. 1978, ApJ, 224, 132
Ferrière, K. 2012, A&A, 540, A50
Frisk, U., Hagström, M., Ala-Laurinaho, J., et al. 2003, A&A, 402, L27
Herrnstein, R. M., & Ho, P. T. P. 2005, ApJ, 620, 287
Hollenbach, D., Kaufman, M. J., Bergin, E. A., & Melnick, G. J. 2009, ApJ, 690, 1497
Karlsson, R., Sandqvist, Aa., Hjalmarson, Å., et al. 2013, A&A, 554, A141
Karlsson, R., Sandqvist, Aa., Fathi, K., & Martin, S. 2015, A&A, 582, A118
Lis, D. C., & Carlstrom, J. E. 1994, ApJ, 424, 189
Lis, D. C., Phillips, T. G., Goldsmith P. F., et al. 2010, A&A, 521, L26
Liszt, H. S., Lucas, R., & Pety, J. 2006, A&A, 448, 253
Mezger, P. G., Duschl, W. J., & Zylka, R. 1996, A&ARv, 7, 289
Mills, E. A. C., & Morris, M. R. 2013, ApJ, 772, 105
Morris, M., & Serabyn, E. 1996, ARA&A, 34, 645
Nordh, H. L., von Schéele, F., Frisk, U., et al. 2003, A&A, 402, L21
Persson, C. M., Black, J. H., Cernicharo, J., et al. 2010, A&A, 521, L45
Persson, C. M., De Luca, M., Mookerjea, B., et al. 2012, A&A, 543, A145
Persson, C. M., Hajigholi, M., Hassel, G. E., et al. 2014, A&A, 567, A130
Pineau des Forets, G., Roueff, E., & Flower, D. R. 1990, MNRAS 242, 512
Requena-Torres, M. A., Güsten, R., Weiss, A., et al. 2012, A&A, 542, L21
Sandqvist, Aa. 1989, A&A, 223, 293
Sandqvist, Aa., Bergman, P., Black, J. H., et al. 2003, A&A, 402, L63
Sandqvist, Aa., Larsson, B., Hjalmarson, Å., et al. 2008, A&A, 482, 849
Sandqvist, Aa., Larsson, B., Hjalmarson, Å., et al. 2015, A&A, 584, A118
Sofue, Y. 1995, PASJ, 47, 527
van der Tak, F. F. S., Black, J. H., Schöier, F. L., Jansen, D. J., & van Dishoeck, E. F. 2007, A&A, 468, 627
Walmsley, C. M., Güsten, R., Angerhofer, P., & Mundy, L. 1986, A&A, 155, 129
Wirström, E. S., Bergman, P., Black, J. H., et al. 2010, A&A, 522, A19